

# Crystalline Plasticity on Copper (001), (110), and (111) Surfaces during Nanoindentation

Haiyi Liang<sup>1</sup>, C.H. Woo<sup>1,2</sup>, Hanchen Huang<sup>3</sup>, A.H.W. Ngan<sup>4</sup>, and T.X. Yu<sup>5</sup>

**Abstract:** Molecular dynamics (MD) simulations are performed to study crystalline plasticity during nanoindentation by comparing the elastic-plastic response of three copper substrates with surfaces (001), (110), and (111) crystallographic planes. The effects of elastic anisotropy and crystallographic symmetry on the reduced modulus, dislocation nucleation, and subsequent microstructure evolution, are investigated. The reduced modulus of (111) surface is found to be the largest, while that of (001) surface is the smallest. Elastic stress distribution calculated from finite element method (FEM) is qualitatively consistent with the MD simulation results. Significant differences exist in the deformation behavior in the three different crystallographic orientations. The differences in the load-displacement curves for the three different cases are correlated with those in the corresponding evolutions of the underlying dislocation structure. Yielding platforms exist typically in load-displacement curve of Cu (001), which can be attributed to effective resistance of dislocation locks. Load drops are typically characteristic of Cu (111) and (110), due to a more mobile dislocation structure.

**keyword:** nanoindentation, molecular dynamics, anisotropy.

## 1 Introduction

Due to the rapid development of nanotechnology in recent years, the understanding of the mechanical properties of solids in the nanoscale is of technological im-

portance, besides the obvious scientific interest. Gane and Bowden (1968) first reported that gold samples could sustain stresses, induced by indentation on a small scale, approaching the theoretical shear strength, despite the likely presence of dislocations beneath the indenter prior to the onset of the strain burst. With the development of powerful instruments in recent years, such as atomic force microscope (AFM), and interfacial force microscope (IFM), structures and events at atomistic scale becomes accessible and more detailed information of the deformation mechanisms at the nanoscale have been obtained with atomic resolution.

The study of crystalline effects on plasticity has a long history. The advent of experimental and modeling techniques in the nanoindentation area offers new opportunities in the investigation of this important problem. [Ghoniem and Cho(2002); Srivastava and Atluri (2002)] Indeed, the experimental works by Keily and Houston (1998), and Corcoran, Colton, Lilleodden, and Gerberich (1997), on gold showed that the effect of crystallography anisotropy is an important factor responsible for the complex behavior of its deformation during nanoindentation. However, due to the many factors that may affect plastic behavior under nanoindentation, such as the size and tip geometry of the indenter, penetration depth, surface oxide layer and contamination, time-dependent characteristics, and strain gradient effects etc., a straightforward interpretation of nanoindentation measurements is difficult [Gouldstone, Koh, Zeng, Giannakopoulos, and Suresh (2000), Swadener, George, and Pharr (2002), Chiu and Ngan (2002), and Gerberich, Tymiak, Grunlan, Horstemeier, and Baskes (2002)].

To complement the experiments to better understand the mechanics of plastic deformation during nanoindentation, atomistic simulations have contributed a substantial portion of the knowledge of the nucleation and evolution of microstructure during nanoindentation, especially in the initial stage. Kelchner, Plimpton, and

<sup>1</sup> Department of Electronic and Information Engineering, Hong Kong Polytechnic University, Hong Kong SAR, China

<sup>2</sup> Communicating author. (Fax: +852-2365-4703, E-mail: chung.woo@polyu.edu.hk)

<sup>3</sup> Department of Mechanical, Aerospace & Nuclear Engineering, Rensselaer Polytechnic Institute, Troy, NY 12180, USA

<sup>4</sup> Department of Mechanical Engineering, University of Hong Kong, Hong Kong SAR, China

<sup>5</sup> Department of Mechanical Engineering, Hong Kong University of Science and Technology, Hong Kong SAR, China

Hamilton (1998) used molecular dynamics to simulate displacement-controlled indentation on the Au (111) surface, and observed dislocation loops appearing off the indenter axis, when the applied shear stress was much beyond the critical shear stress. Via MD simulation, Zimmerman, Kelchner, Klein, Hamilton, and Foiles (2001) found a significant decrease in the load to nucleate dislocations due to surface step effects. Rodrigue, Zimmerman, González, Figuera, Hamilton, Pai, and Rojo (2002) simulated the formation of hillocks near indentation points, and found that the hillocks were composed of four Shockley partials and a stair-rod dislocation. By combining the results of atomistic and finite-element modeling, Li, Vliet, Zhu, Yip, and Suresh (2002), related the concept of structural stability and the nucleation of defects during nanoindentation in their interpretation of experiments. Recently, with quasi-continuum method, Knap and Ortiz (2003) found that, with an indenter of tip radius 70 nm, there is no force drop despite the existence of profuse dislocation activity.

Although MD simulations of nano-indentation have been reported by many authors in the literature, a systemic study of the crystalline anisotropy effects on nanoindentation and the detailed underlying dislocation evolution is still lacking. In the present paper, we perform MD simulations of nano-indentation on Cu (001), (110), and (111) surfaces. The marked crystalline anisotropy exhibited by the elasticity of copper, plus its readily available and relatively reliable inter-atomic potential, makes it a prime candidate for the study of crystalline effects of nanoplasticity via atomistic simulation. Our aim is to gain insight into the relationships between the displacement-load behavior and the concomitant development of the dislocation structures during nanoindentation. Comparison of the results on various crystalline surfaces reveals the difference in the development of incipient plasticity in non-equivalent crystallographic directions.

## 2 Simulation Procedure

Three copper substrates with (001), (110), and (111) surfaces are modeled as slabs. For Cu (001), the dimension is  $188 \times 188 \times 108 \text{ \AA}^3$  (containing 324,480 atoms), the top free surface is (001) plane, and the other two side surfaces are (100) and (010) respectively. For Cu (110), the dimension is  $189 \times 187 \times 112 \text{ \AA}^3$  (containing 338,624 atoms), and the top surface is (110) plane with the other two side surfaces ( $\bar{1}10$ ) and (001) respectively. For Cu

(111), the dimension is  $190 \times 189 \times 112 \text{ \AA}^3$  (containing 341,334 atoms), and the top surface is (111) plane with the other two side surfaces ( $\bar{1}10$ ) and ( $\bar{1}\bar{1}2$ ) respectively.

In all cases, periodic boundary conditions are applied along the horizontal directions. The top surface is traction free, and the atomic layers of two cutoff distances at the bottom are held fixed. The temperature of the simulation cell (i.e., all the moving atoms) is kept constant at 300K through Nosé-Hoover thermostat. Following Kelchner, Plimpton, and Hamilton (1998), a repulsive potential is used to model a spherical indenter made of a material like tungsten, with a radius of  $R = 40 \text{ \AA}$ .

The EAM potential of Doyama and Kogure (1999) for copper is used for the substrate. The parameters are determined from the experimental data of cohesive energy, Born stability, elastic constants  $C_{11}, C_{12}$  and  $C_{44}$ , formation energy of a vacancy, and stacking fault energy ( $35.7 \text{ mJ/A}^2$ ). The indentation velocity we use is about 3 m/s, which is nine orders of magnitude higher than the experimental ones. This excessively large indenting velocity is an intrinsic problem of MD. Even this 3m/s is already an order of magnitude slower than those used in the past, 40 m/s by Christopher, Smith and Richter (2001), and the 50 m/s by Gannepalli and Mallapragada (2002). The sensitivity of the simulation results to the indentation velocity has been discussed by Liang, Woo, Huang, Ngan, and Yu (2003). The relationship between the applied load and the indentation depth remains little changed, although a higher indentation velocity in MD simulation leads to a higher strength. At the same time, the associated dislocation structures are also left essentially unaffected. More importantly, the values will quickly converge as the velocity decreases. Indeed, our results show no obvious difference at a velocity below 3 m/s. Nevertheless, one must be aware that convergence within MD here does not necessarily mean that time-dependent mechanisms, such as diffusion driven ones, have been properly included.

To correlate the load-displacement behavior with the dislocation structure evolution beneath the indenter, following Zimmerman, Kelchner, Klein, Hamilton, and Foiles (2001), we identify dislocation structures with the help of a slip vector defined as

$$\mathbf{s}^\alpha = -\frac{1}{n_s} \sum_{\beta \neq \alpha}^n (\mathbf{x}^{\alpha\beta} - \mathbf{X}^{\alpha\beta}) \quad (1)$$

where  $\mathbf{x}^{\alpha\beta}$  and  $\mathbf{X}^{\alpha\beta}$  are the vectors linking atom  $\alpha$  and

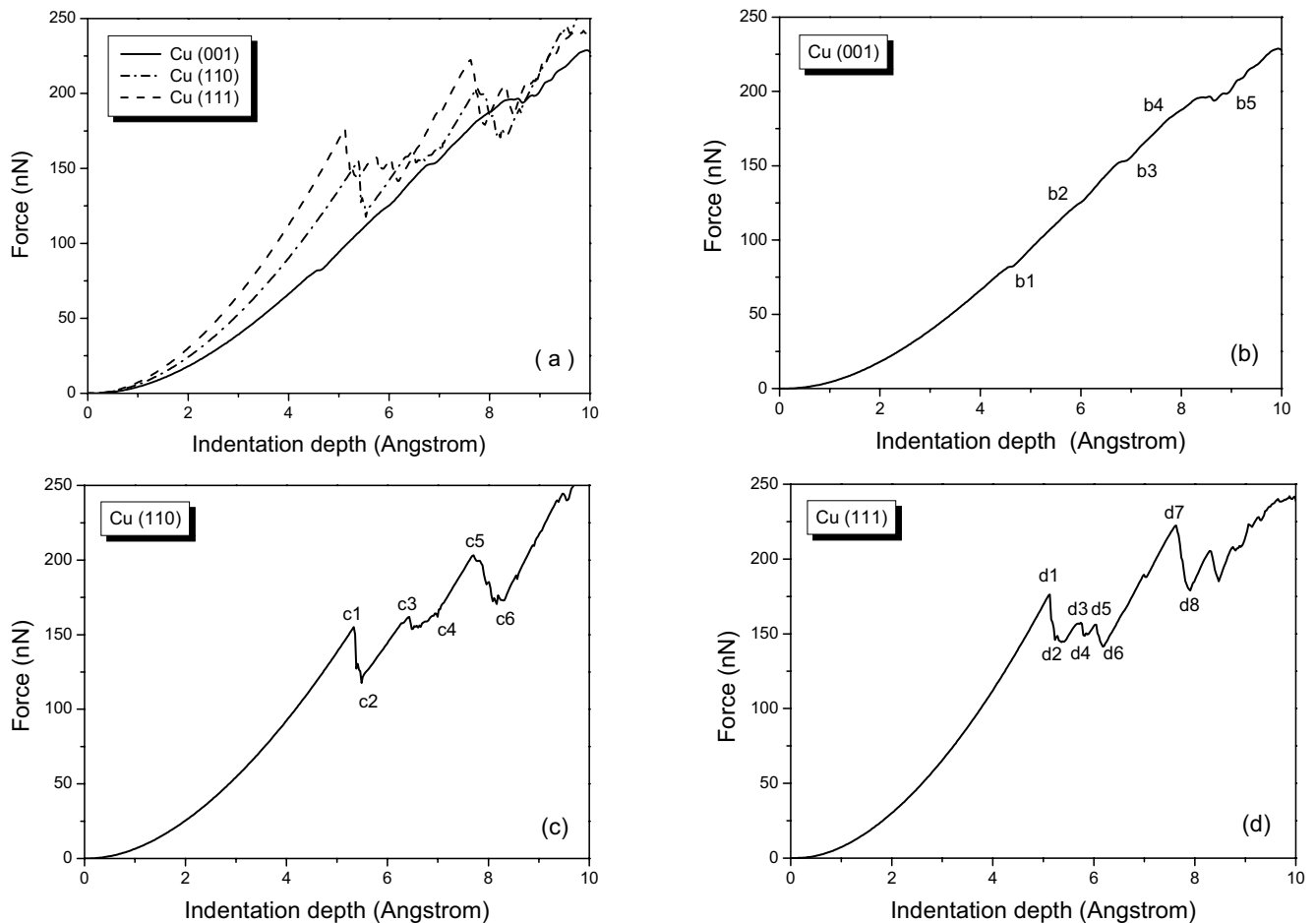


**Figure 1** : Load-displacement curve of Cu (001), (110), and (111).

all its nearest neighbors  $\beta$  in the current and reference position,  $n_s$  being the number of slipped neighbors. In the following, atoms with slip vectors having a magnitude  $|\mathbf{s}^\alpha|$  ranging from 0.1 to 3.0 Å are displayed. The atoms are colour coded according to the magnitude of the slip vectors. Areas containing atoms identified with significant slip vectors usually denote the presence of faults in the stacking, indicating the existence of faulted loops, or the extended core of split dislocations, in which the partials are situated at the edge of the faulted area. We find this a clear and convenient way of illustrating the elastic and plastic response of the substrate during loading.

### 3 Results and Discussion

#### 3.1 Elastic regime

The nanoindentation load-displacement curves, i.e., force ( $F$ ) vs. indentation depth ( $h$ ), of copper on crys-

tallographic surfaces (001), (110), and (111) are compared in Fig.1.  $F$  is the load applied to press the indenter. The indentation depth ( $h$ ) is the prescribed displacement of the indenter, which is related to the movement of the spherical indenter center. We note that the actual depth is smaller than the prescribed indenter displacement due to the compliance of the repulsive indenter.

Fig.1a shows the strong effects of the crystallographic anisotropy on the reduced modulus along different crystallographic directions. According to the Hertz theory, the load vs. depth behavior of an isotropic elastic media follows

$$F = \frac{4}{3} E^* R^{1/2} h^{3/2} \quad \frac{1}{E^*} = \frac{1 - \nu_{sub}^2}{E_{sub}} + \frac{1 - \nu_{ind}^2}{E_{ind}} \quad (2)$$

where  $E^*$  is the reduced modulus, a combination of the elastic modulus  $E_{sub}$  and  $E_{ind}$  and Poisson's ratios  $\nu_{sub}$  and  $\nu_{ind}$  of the substrate and the indenter respectively, and

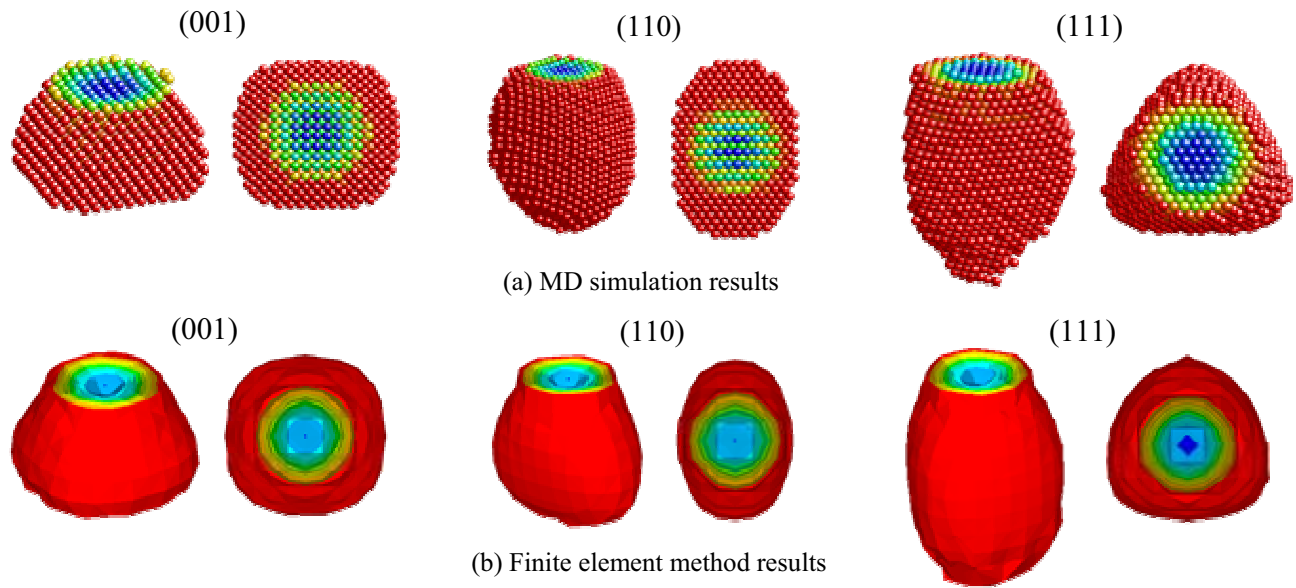


**Figure 2** : Stress  $\sigma_z$  under indenter, calculated from (a) MD simulation and (b) Finite element method. For each case, the left picture is side-view, and the right is top view. Only atoms having  $|\sigma_z| > 4\text{GPa}$  are plotted.

$R$  is the indenter radius.

Using values of  $F$  and  $h$  read off directly from Fig.1a, the reduced modulus can be calculated using equation (2). For  $h=2.0\text{\AA}$ , we obtain values of  $E^*$  of 75.7GPa, 101.8GPa, and 123.4GPa for Cu (001), (110), and (111), respectively.

We note that, strictly speaking, equation (2) is only applicable to an isotropic medium. The foregoing results are thus only qualitatively valid for the anisotropic copper substrates presently under consideration. Assuming a tungsten-like indenter with  $E_{ind}=400\text{GPa}$ ,  $\nu_{ind}=0.28$ , and Young's modulus for the copper substrate of  $E_{001}=77.5\text{GPa}$ ,  $E_{110}=137.0\text{GPa}$ , and  $E_{111}=191.9\text{GPa}$ , calculated from the Doyama-Kogure potential, and Poisson's ratio  $\nu_{sub}=0.3$ , the reduced modulus from equation (2) are calculated to be  $E_{001}^*=71.2\text{GPa}$ ,  $E_{110}^*=111.7\text{GPa}$ , and  $E_{111}^*=141.9\text{GPa}$ . These agree reasonably well with the values obtained directly from the load-displacements curves.

Using the theoretical method proposed by Vlassak and Nix (1994), the reduced modulus for copper (001), (110), and (111) are 108.8GPa, 114.2GPa, and 115.9GPa respectively, with elastic constants from Doyama-Kogure potential. The theoretical predication shows much less anisotropic effect than our simulation. Stronger elastic anisotropy effects were also observed in MD simu-

lation and experiment [Lilleodden, Zimmerman, Foiles, and Nix (2003), Kiely and Houston (1998)]. We note that the model of Vlassak and Nix (1994) considered the elastic response of substrate under a pyramidal indenter during unloading, in the presence of full plasticity. In the present paper, on the other hand, we consider the early part of the loading stage, with a fully elastic substrate under spherical indenter, using the Hertz theory. Despite the difference of elastic anisotropy effects in MD simulation, experiments, and theoretical method, all studies show that the (111) surface has the largest reduced modulus while (001) surface is the softest.

Apart from the effects on the reduced modulus, the elastic anisotropy also influences the stress distribution under the indenter. In Fig.2a, we show the top- and the side-views of the spatial dependence of the  $\sigma_z$  component (along indentation direction), using atomic stress tensor [Egam, Maeda, and Vitek (1980)], in the elastic regime for each of the three indentation directions. The stress distributions exhibit strong anisotropy, showing  $90^\circ$  rotational symmetry in Cu (001),  $180^\circ$  rotational symmetry in Cu (110), and  $120^\circ$  rotational symmetry in Cu (111). While for an isotropic media, the stress field under the indenter is axisymmetric, in comparison.

Three-dimensional analysis using finite element method (FEM) for a stiff frictionless spherical indenter press-

ing onto substrates corresponding to Cu (001), (110), and (111), is performed with the ANSYS software. The stresses  $\sigma_z$  are shown in Fig.2b, in comparison with the MD results in Fig.2a. Despite the difference between the MD and the FEM models, in the indenters used and the assumption regarding the elastic linearity, the qualitative resemblance between FEM and MD results shows the consistency of both calculations. It also suggests that, in the elastic regime, the discrete lattice can still be described satisfactorily as a continuum, despite the highly concentrated local stresses. One may even speculate that the potential sites of dislocation nucleation in a single crystal can be predicated by FEM, by analyzing for elastic instability [Li, Vliet, Zhu, Yip, and Suresh (2002)].

Since the FEM results can be scaled arbitrarily, for a large indenter, the stressed volume increases accordingly, and the nucleation site also moves deeper into the substrate. The increased volume may be sufficiently large to accommodate the simultaneous generation of several dislocations once the critical stress is attained.

### 3.2 Incipient plasticity

In the following, we describe the different load-displacement relations of the indentation in the three crystallographic orientations (Fig.1). The concomitant microstructure development and deformation mechanisms will be considered in the next subsection. In all cases, the load-displacement relations are characterized by a smooth steady elastic region, beyond which inflexion points signaling the occurrence of plasticity can be seen.

For Cu (001) (Fig.1b), there are five inflexion points produced by minor yielding due to steady inelastic deformation under the indenter. Between the inflexion points, the curve shows a relatively stable and smooth quasi-elastic behavior, corresponding to a steady buildup of internal stress, consistent with a relatively inactive dislocation structure. The magnitude of the inelastic displacements (or yielding platforms) at points #b1, #b3, and #b5 (Fig.1b) are 0.06, 0.13 and 0.60 Å respectively, indicating an increasing magnitude of the underlying dislocation activities, as the indenter advances. Lilleodden et al. (2003) found small load drops for (001) Au instead of yielding platforms. This is somewhat different from our results, but may be attributed to the difference in the hardness of indenter, atom potentials, and simulation conditions adopted in either case. Nevertheless, the

large load drop they found for (111) Au is essentially the same as our case.

Instead of yielding platforms as in Cu (100), the most prominent feature of the load-displacement curve of Cu (110) are large load drops (Fig.1c), at points #c1 ( $h \sim 5.3$  Å and  $F \sim 155.0$  nN), #c3 ( $h \sim 6.4$  Å and  $F \sim 161.5$  nN) and #c5 ( $h \sim 7.6$  Å and  $F \sim 203.2$  nN). These occur due to a sudden relaxation of the internal stress supporting the indenter, such as caused by a sudden burst of dislocations from a source. It is also noted that the relaxation here is associated only with a relatively small advancement of the indenter. Between the points #c3 and #c4 there is a yielding platform preceded by a small stress relaxation, in which relatively large indenter advancement occurs, probably caused by dislocation glide driven by the applied shear against some barriers. The steadily rising parts of the curve between points #c2 and #c3, #c4 and #c5, and after point #c6 exhibit the typical quasi-elastic behaviour, corresponding to the accumulation of internal stresses, caused by the formation of a relatively inactive dislocation structure, such as locks, at #c2 and #c6.

The load-displacement curve of Cu (111) in Fig.1d bears much more similarity to Cu (110) than to Cu (100). The outstanding features are also large load drops with little deformation at points #d1 ( $h \sim 5.1$  Å and  $F \sim 176.3$  nN) and #d7 ( $h \sim 7.6$  Å and  $F \sim 222.1$  nN), caused by the relaxation of an overstressed crystal through a sudden burst of dislocation activities. The region between points #d2 and #d6 behaves in a way similar to Cu (110) between #c3 and #c4, namely a yielding stage that involves a small stress relaxation, but a relatively large indenter advancement, probably caused by dislocation glide under a constant driving shear. Between points #d6 and #d7, the curve rises again quasi-elastically, with a minor inflexion, corresponding to the accumulation of internal stress, caused by a relatively inactive dislocation structure.

In the forgoing, it is noted that, independent of the crystallographic direction of the indentation, three types of features can be identified in the load displacement curves: (1) a quasi-elastic regime; (2) sudden load drops; and (3) displacement under constant load (simply called strain burst). This is in complete agreement with experimental observation in which discrete load jump or strain burst with intermittent elastic responses is typical [Suresh, Nieh, and Choi (1999), Kiely, Jaraush, Houston, and Russell (1999)]. Despite the commonality, com-

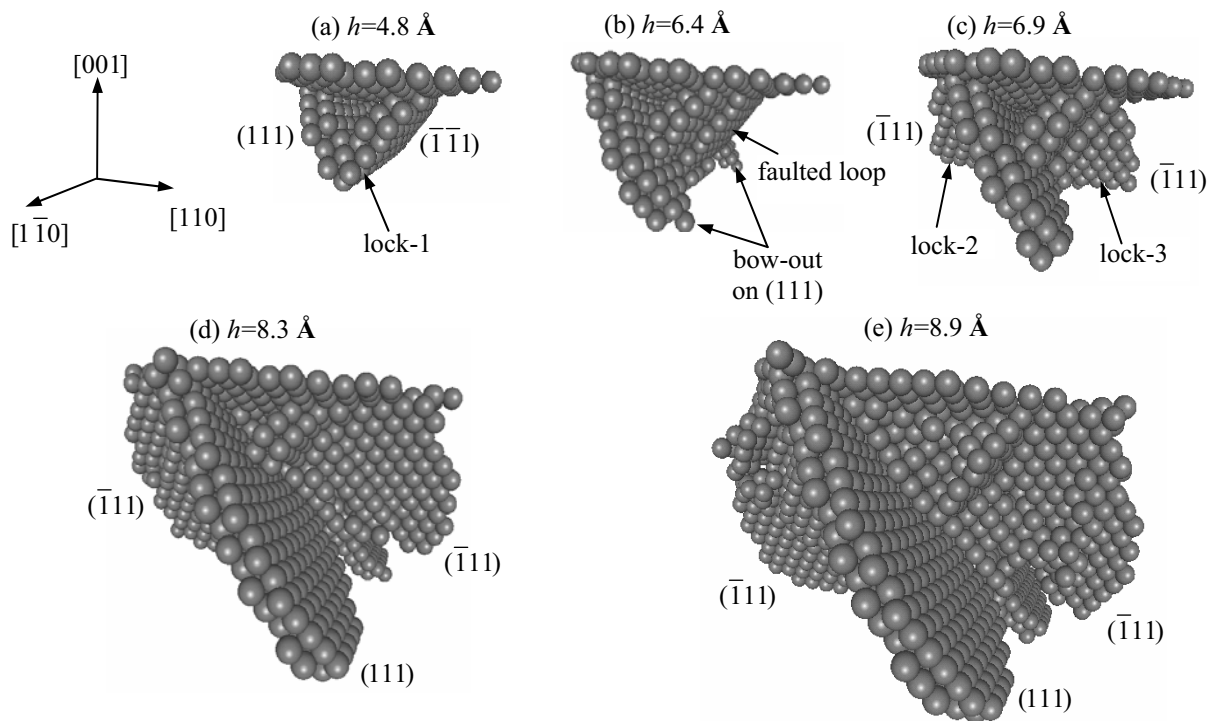


**Figure 3** : Microstructure evolution beneath the contact surface on Cu (001)

parison of the load-displacement curves in Fig.1b-d reveals significant differences in the deformation behavior during nanoindentation in the three different crystallographic directions. While all three types of features are present in the case of Cu (111) and (110), indicating the evolution of a strongly active dislocation structure, quasi-elastic behavior dominates the load-displacement relationship of Cu (001), interrupted only by a few small strain bursts, suggesting a less active movement of underlying dislocation. To achieve a mechanistic understanding of the foregoing stress-strain relationship in terms of the underlying dislocation structure, the microstructure development during the indentation is considered in the following subsection.

### 3.3 Microstructure development

#### 3.3.1 Cu (001)

During the early part of the loading curve, i.e., prior to point #b1 in Fig.1b, no dislocations are identified, which suggests that the substrate is deforming elastically. As the indentation depth increases beyond  $\sim 4.8 \text{ \AA}$  (point #b1 in Fig.1b), a pair of Shockley partials, on (111) and  $(\bar{1}\bar{1}\bar{1})$  slip planes (Figs. 3a), are nucleated beneath the

contact surface. The Shockley partial pair grows to intersect with the surface, and with each other forming a stair-rod dislocation and a Lomer-Cottrell lock (lock-1) from the dislocation reaction  $\frac{1}{6}a[\bar{1}\bar{1}2] + \frac{1}{6}a[\bar{1}\bar{1}\bar{2}] = \frac{1}{3}a[\bar{1}\bar{1}0]$  ( $a$  is the lattice constant of copper). After the lock is formed, the crystal hardens, as reflected by the resumption of loading. The presence of lock-1 restricts the plastic flow of the material inside the wedged-shape region bounded by the two  $\{111\}$  slip planes, and therefore hardens the material inside the wedge. The load transmitted by the indenter through the wedge creates a stress concentration at its tip, which generates the nucleation of a pair of faulted loops at both ends of the Lomer-Cottrell lock, resulting in the minor yield at point #b2 (Fig.1b). When the formation of the faulted loops completes, the quasi-elastic behavior after point #b2 (Fig.1b) resumes.

When the contact area gets bigger as the loading continues, i.e., between points #b1 and #b3 (Fig.1b), the increase of local stress forces the unlocked non-edge segments on one of the Shockley partial pair to bow out, expanding the faulted area on the (111) plane (Fig.3b, 3c). Just at point #b3 in Fig.1b, two new Lomer-Cottrell locks (lock-2 and lock-3, in Fig.3c) come into being, perpendicular to lock-1. The processes of Shockley partial

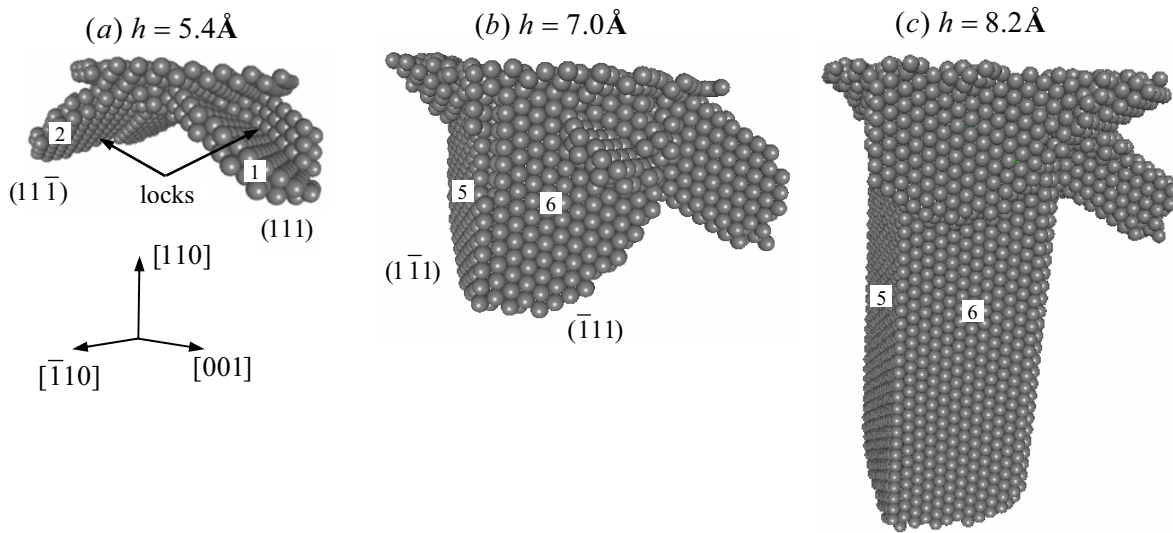


**Figure 4 :** The side view of microstructure evolution beneath the contact surface on Cu (110)

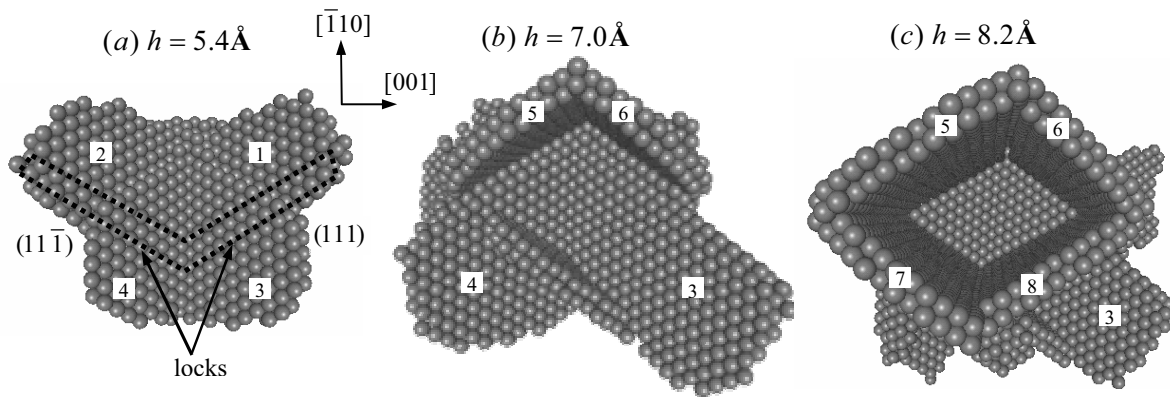


**Figure 5 :** The bottom view of microstructure evolution beneath the contact surface on Cu (110)

bow-out and formation of new locks contribute to the minor yield at point #b3 (Fig.1b).

After the formation of lock-2 and lock-3, the yielding is interrupted and the load displacement curve resumes its quasi-elastic behavior between points #b3 and #b4. At this point, different parts of the substrate deform via different mechanisms, some elastically, some via the dislocation bow out on the (111) plane, and some via the nucleation and growth of Shockley partials. The resultant effect produces the quasi-elastic behavior on the load-displacement curve between points #b3 and #b4 (Fig.1b).

Beyond point #b4 (Fig.1b), the expansion of the contact area drives the bow out of the non-edge segments on lock-2 and lock-3 on the  $(\bar{1}\bar{1}1)$  faulted plane (Fig.3d), then producing major plastic deformation at point #b5

(Fig.1b). The large excursions beyond point #b5 correspond to the usual cold-working process, in which dislocations are generated, interact, and form locks.

Despite the weaker strength in [100] direction, the repeated formation of locks thwarted attempts of the crystal to relax the stresses accumulated as the indentation proceeds. As a result, the load-sustaining capability to nanoindentation in this direction is comparable to the other directions (Fig.1b-d).

### 3.3.2 Cu (110)

The development of microstructure during indentation on Cu (110) is shown in Fig.4a-c, the bottom views of which are shown in Fig.5a-c. As the indentation depth increases beyond  $\sim 5.4 \text{ \AA}$  (point #c1 in Fig.1c), a Shockley par-

tial embryo starts first to grow on plane #1 (Fig.4a, 5a), which triggers the subsequent unsymmetrical nucleation of the other three partials on plane #2, #3, and #4 (Fig.4a, 5a). Planes #1 and #3 are two adjacent (111) planes, and planes #2 and #4 are two adjacent (11 $\bar{1}$ ) planes. During the same period, two other partials nucleate on ( $\bar{1}$ 11) and (1 $\bar{1}$ 1) planes, intersect with the partials on planes #1 and #2 respectively, and form two Lomer-Cottrell locks (Fig.4a, 5a). Unlike the Lomer-Cottrell lock in Fig.3a, the lock here is not effective enough to prevent the further movement of dislocations. The nucleation and development of the above structure leads to a sudden load drop at #c1 (Fig.1c), and the resumption of quasi-elastic behavior at #c2 is due to the formation of the locks. From point #c2 to #c3 (Fig.1c), the indentation strain is accommodated elastically, with a corresponding accumulation of the stress. There is not much evolution of the dislocation structure between #c2 and #c3 (Fig.4a).

As the stress continues to accumulate, the dislocation structure starts to change at point #c3, leading to the load drop at this point. From point #c3 ( $\sim 6.5$  Å) to #c4 ( $\sim 7.0$  Å) in Fig.1c, the dislocations becomes very active, and the original dislocation structure as represented by Fig.4a change dramatically. Dislocation on plane #3 grows much larger than that on plane #4, while those on planes #1 and #2 shrink back and almost vanish. New locks are formed preventing further movement. Most notably, two new dislocations, nucleated on (1 $\bar{1}$ 1) (plane #5) and ( $\bar{1}$ 11) (plane #6) respectively, intersecting and locked with each other, stem downwards from under the (110) surface (Fig.4b, 5b).

The load-displacement relation between points #c4 to #c5 (Fig.1c) is essentially elastic, similar to the elastic behavior between points #c2 and #c3 (Fig.1c). The shape of underlying dislocation structure again remains almost unchanged from point #c4 to #c5 in Fig.1c.

At point #c5 in Fig.1c, a large load drop occurs as two new dislocations nucleate on ( $\bar{1}$ 11) (plane #7) and (1 $\bar{1}$ 1) (plane #8), and intersect with the previous dislocations on planes #5 and #6 to form a prismatic dislocation loop gliding away from the surface (Fig.4c, 5c) and stop at a point where stress due to the indentation is sufficiently diminished. Here, we point out that there is one prismatic dislocation at the bottom end of the square pipe, the left part of which is the trace this dislocation left. As envisioned by Suresh, Nieh, and Choi (1999), the periodical punching of prismatic dislocation into substrate might

be one cause of strain burst. Additionally, this prismatic dislocation can be regarded as geometrically necessary dislocation (GND), accommodating those atoms pushed into substrate by indenter (Gao and Huang, 2003).

### 3.3.3 Cu (111)

The development of microstructure during indentation on Cu (111) is shown in Fig.6a-d. As the indentation depth increases beyond the elastic regime at  $\sim 5.1$  Å (point #d1 in Fig.1d), a Shockley partial embryo starts to appear on (1 $\bar{1}$ 1) (plane #1), followed by the nucleation and development of Shockley partial on (11 $\bar{1}$ ) (plane #2 in Fig.6a). The two partial dislocations intersect with each other to form a Lomer-Cottrell lock (pointed by arrow in Fig.6a). The dislocation structure in Fig.6a is the same as that shown by Lilleodden, Zimmerman, Foiles, and Nix (2003), with stacking fault near the free edges, and a perfect lattice near the top of the intersection of plane #1 and #2. Similar to Cu (110), the current lock can only offer weak resistance to the movement of existing dislocations. As a result, the associated dislocation activity is responsible for the large load drop between #d1 and #d2 in Fig.1d.

The wavy yielding region, from point #d2 to #d6 in Fig.1d, involves a sequence of minor but distinct local rearrangement of the dislocation structure. At point #d4 (Fig.6b,  $\sim 5.8$  Å), a new partial dislocation nucleates on ( $\bar{1}$ 11) (plane #3), which subsequently intersects with former dislocations on planes #1 and #2 to form a stable tetrahedron defect structure beneath the indenter. In comparison, a pyramidal defect structure has been observed in a MD simulation with a truncated pyramid indenter (Gannepalli and Mallapragada 2002). Similar to the wedged-shape dislocation structure in Fig.3a, this tetrahedron structure here serves as a source of stress concentration. Dislocation loops (for instance, partial dislocations on ( $\bar{1}$ 11), (1 $\bar{1}$ 1) and (11 $\bar{1}$ ) planes, namely planes #4, #5 and #6 in Fig.6b, 6c) are forced out along the “walls” of the tetrahedron (Fig.6b, 6c). These intensive dislocation activities are completed at point #d6 in Fig.1d ( $\sim 6.2$  Å, Fig.6c). The intensive local atom movement leads to continuous stress relief. Therefore, the substrate undergoes large deformation between #d2 and #d6 without a significant build-up of stress. It is worth pointing out that in this process, dislocations nucleated out of the tetrahedron will grow or shrink according to local stress variation.

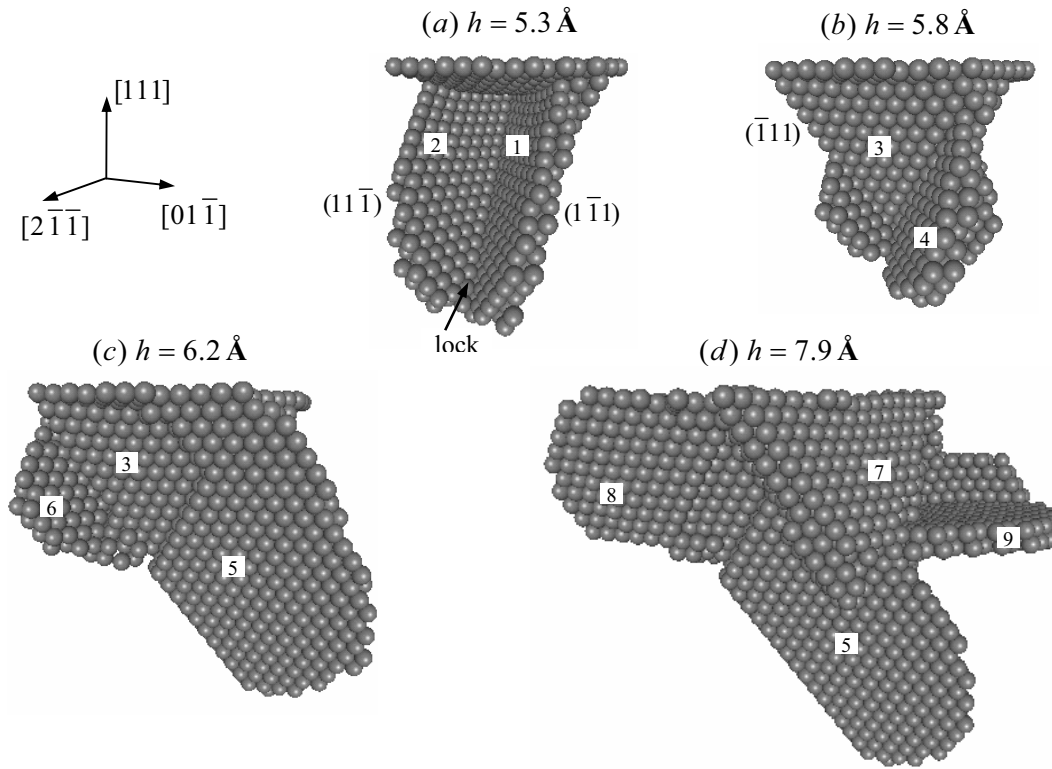


**Figure 6 :** Microstructure evolution beneath the contact surface on Cu (111)

At the stable stage from point #d6 to #d7 (Fig.1d), the dislocation structures grow a little, without essential difference in shape from that in Fig.6c. At point #d8 in Fig.1d ( $\sim 7.9 \text{ \AA}$ ), a large load drop occurs, which can be attributed to intensive dislocation activities, i.e. nucleation and development of partial dislocations on planes #7~#9, around the tetrahedron (Fig.6d). It is interesting to note that a dislocation nucleates horizontally on (111) (plane #9).

#### 4 Summary

In this paper, molecular dynamics simulations of nano-indentation are performed to study the elastic anisotropy effects on the elastic-plastic deformation on copper (001), (110) and (111) surfaces. The evolution of the underlying dislocation structure is correlated with the load-displacement relation.

Due to elastic anisotropy, the reduced modulus of (111) surface is found to be the largest, while that of (001) the smallest. The normal stress distribution beneath the indenter shows different rotational symmetry. It is interesting to find that stress tensors calculated from finite el-

ement method and molecular dynamics are qualitatively the same, despite the distinctly discrete nature of lattice at such small scales.

In all three cases, the load-displacement relations are characterized by repetition of a smooth region (indicating a stable crystalline structure) followed by yielding platform or load drop (signaling intensive dislocation activities).

For Cu (001), due to the effective resistance of Lomer-Cottrell lock to further movement of dislocation, only yielding platform tends to appear. For Cu (110) and (111), despite the existence of profuse lock formation, dislocations are subjected to much weaker resistance than for Cu (001), which results in frequent load drop. In addition, a geometrically necessary dislocation is observed for Cu (110) responsible for a large force drop.

**Acknowledgement:** The work described in this paper was supported by grants from the Research Grants Council of the Hong Kong Special Administrative Region (PolyU 1/99C, PolyU 5309/03E and PolyU 5312/03E).

## References

- Chiu, Y. L.; Ngan, A.H.W.** (2002): Time-dependent characteristics of incipient plasticity in nanoindentation of a Ni<sub>3</sub>Al single crystal, *Acta Mater.*, Vol. 50, pp.1599-1611.
- Corcoran, S. G.; Colton, R. J.; Lilleodden, E. T.; Gerberich, W. W.** (1997): Anomalous plastic deformation at surfaces: nanoindentation of gold single crystals, *Phys. Rev. B*, Vol. 55, No. 24, pp.16057-16060.
- Christopher, D.; Smith, R.; Richter, A.** (2001): Atomistic modeling of nanoindentation in iron and silver, *Nanotechnology*, Vol. 12, pp.372-383.
- Doyama, M.; Kogure, Y.** (1999): Embedded atom potentials in fcc and bcc metals, *Comp. Mat. Sci.*, Vol. 14, pp.80-83.
- Egami, T.; Maeda, K.; Vitek, V.** (1980): Structural defects in amorphous solids - a computer simulation study, *Phil. Mag. A*, Vol. 41, No. 6, pp.883-901.
- Gane, N.; Bowden, F. P.** (1968): Microdeformation of solid, *J. Appl. Phys.*, Vol. 39, No. 3, pp.1432-1435.
- Gannepalli. A.; Mallapragada. S. K.** (2002): Atomistic studies of defect nucleation during nanoindentation of Au (001), *Phys. Rev. B.*, Vol. 66, pp.104103-104111.
- Gao, H. J.; Huang, Y. G.** (2003): Geometrically necessary dislocation and size-dependent plasticity, *Script. Mater.*, Vol. 48, pp.113-118.
- Gerberich, W. W.; Tymiak, N. I.; Grunlan, J. C.; Horstemeyer, M. F.; Baskes, M. I.** (2002): Interpretations of indentation size effects, *J. Appl. Mech.*, Vol. 69, pp.433-441.
- Ghoniem, N. M.; Cho, K.** (2002): The emerging role of multiscale modeling in nano- and micro-mechanics of materials. *CMES: Computer Modeling in Engineering & Sciences*, vol. 3, no. 2, pp. 147-174.
- Gouldstone, A.; Koh, H. J.; Zeng, K. Y.; Gianakopoulos, A. E.; Suresh, S.** (2000): Discrete and continuous deformation during nanoindentation of thin films, *Acta Mater.*, Vol. 48, pp.2277-2295.
- Kelchner, C. L.; Plimpton, S. J.; Hamilton, J. C.** (1998): Dislocation nucleation and defect structure during surfaces indentation, *Phys. Rev. B*, Vol. 58, No.17, pp.11085-11088.
- Kiely, J. D.; Houston, J. E.** (1998): Nanomechanical properties of Au (111), (001), and (110) surfaces, *Phys. Rev. B*, Vol. 57, No. 19, pp.12588-12594.
- Kiely, J. D.; Jaraush, K. F.; Houston, J. E.; Russell, P. E.**, (1999): Initial stages of yield in nanoindentation, *J. Mater. Res.*, Vol. 14, No. 6, pp.2219-2227.
- Knap, J.; Ortiz, M.** (2003): Effect of indentation-radius size on Au (001) nanoindentation, *Phys. Rev. Lett.*, Vol. 90, No. 22, pp.226102-226105.
- Li, J.; Van Vliet, K. J.; Zhu, T.; Yip, S.; Suresh, S.** (2002): Atomistic mechanisms governing elastic limit and incipient plasticity in crystals, *Nature*, Vol. 418, pp.307-310.
- Liang, H. Y.; Woo, C. H.; Huang, H. C.; Ngan, A. H. W.; Yu, T. X.** (2003): Dislocation Nucleation in the Initial Stage During Nanoindentation, *Philos. Mag.*, Vol. 83, No.31-34, pp.3609-3622.
- Lilleodden, E. T.; Zimmerman, J. A.; Foiles, S. M.; Nix, W. D.** (2003): Atomistic simulations of elastic deformation and dislocation nucleation during nanoindentation, *J. Mech. Phys. Solids*, Vol. 51, No.5, pp.901-920.
- Rodríguez de la Fuente, O.; Zimmerman, J. A.; González, M. A.; de la Figuera, J.; Hamilton, J. C.; Pai, W. W.; Rojo, J. M.** (2002): Dislocation emission around nanoindentation on a (001) fcc metal surface studied by scanning tunneling microscopy and atomistic simulations, *Phys. Rev. Lett.*, Vol. 88, No. 3, pp.36101-36104.
- Srivastava, D.; Atluri, S. N.** (2002): Computational nanotechnology: A current perspective. *CMES: Computer Modeling in Engineering & Sciences*, vol. 3, no. 5, pp. 531-538.
- Suresh, S.; Nieh, T. G.; Choi, B. W.** (1999): Nanoindentation of copper thin films on silicon substrates, *Script. Mater.*, Vol. 41, No. 9, pp.951-957.
- Swadener, J. G.; George, E. P.; Pharr, G. M.** (2002): The correlation of the indentation size effect measured with indenters of various shapes, *J. Mech. Phys. Solids*, Vol. 50, pp.681-694.
- Vlassak, J. J.; Nix, W. D.** (1994): Measuring the elastic properties of anisotropic materials by means of indentation experiments, *J. Mech. Phys. Solids*, Vol. 42, No. 2, pp.1223-1245.
- Zimmerman, J. A.; Kelchner, C. L.; Klein, P. A.; Hamilton, J. C.; Foiles, S. M.** (2001): Surface step effects on nanoindentation, *Phys. Rev. Lett.*, Vol. 87, No. 16, pp.165507-165510.